Scripta Materialia 212 (2022) 114551

Contents lists available at ScienceDirect

Scripta Materialia

journal homepage: www.elsevier.com/locate/scriptamat

Deformation-driven modification of Al-Li-Mg-Zn-Cu high-alloy aluminum as anodes for primary aluminum-air batteries

Yuming Xie[1], Xiangchen Meng[1], Dongxin Mao, Yuexin Chang, Zhiwei Qin, Xiaotian Ma, Long Wan, Yongxian Huang*

State Key Laboratory of Advanced Welding and Joining, Harbin Institute of Technology, Harbin 150001, China

ARTICLE INFO

Article history:
Received 25 November 2021
Revised 19 January 2022
Accepted 19 January 2022

Keywords:
Aluminum-air batteries
Severe plastic deformation
Anodes
Corrosion

ABSTRACT

Aiming at high-energy-density off-grid application, severe plastic deformation-modified Al-Li-Mg-Zn-Cu high-alloy aluminum obtained by deformation-driven modification was proposed to serve as anodes for primary aluminum-air batteries. Homogeneous microstructures induced by the fragmentation of second phases and dynamic recrystallization suppressed the formation of the hydroxides-eutectic skeletons to isolate anodes from alkaline electrolytes. The alloying elements contributed to the inhibition of hydrogen evolution self-corrosion, the mitigation of polarization, and the enhancement of the discharge voltage. The self-corrosion rate was only one-seventh of the 5N pure aluminum. The power and energy densities reached 88.3 mW cm^{-2} and 2.73 Wh g^{-1}, respectively, which is better than those of pure aluminum.

Carbon neutrality and associated environmental concerns bring about profound demands for renewable energy sources [1]. As the biggest unicorn market of green energy supplies, power cells for electric vehicles and portable devices have been dominated by lithium-ion batteries due to their long cycle life and good energy density [2]. However, their wide applications in off-grid energy supplies and high energy density demands are still restricted due to the destructive issues induced by lithium dendrites and unsafe organic electrolytes [3]. As an old but efficient choice, primary metal-air batteries have received attention to serving as next-generation high-energy off-grid storage systems [4,5]. Among these metal-based cells, aluminum-air batteries are one of the most promising alternatives due to the extraordinary energy densities (8131 Wh kg^{-1}), abundant reserves (the highest metallic abundance), and potential applications in high-value military industries [6–8]. The performances of aluminum anodes strongly depend on the microstructural design and preparing routes [9,10]. Generally, pure aluminum anodes display severe hydrogen evolution reaction (HER) self-corrosion and unstable discharge voltage plateau induced by polarization, leading to a limited anodic efficiency [11]. One straightforward approach to boost the utilization is alloying since the alloying elements can shift the discharge voltage and mitigate self-corrosion [12]. The selection of alloying elements usually meets these criteria: high HER overpotential, good metallurgical compatibility with aluminum, and more positive potential than aluminum [13]. These characteristics are of vital importance to suppress the HER-induced corrosion and the formation of the passivation layers during discharge to provide extraordinary robustness of the aluminum anodes.

High-alloy aluminum (HAA), a combination of high-entropy alloys and aluminum anodes, are capable of combining the advantages of the elements following the above criteria. The utilization of HAA containing active elements (Li [14], Mg [15], etc.) and depolarization elements (Zn [16], In [17], Sn [18], Cu [19], etc.) make it possible to prepare the charming anodes for primary aluminum-air batteries towards high energy density applications. However, due to the serious formation propensity of eutectic microstructures, the HAA containing these low-melting-point elements cannot discharge continuously due to the electrolyte-isolation effect of these eutectic skeletons. This issue results in significant challenges in developing homogeneous anodes [20]. Severe plastic deformation-based techniques show high applicability for homogenizing and refining materials [21–24], which may be suitable for modifying the HAA. Considering this, we utilized the deformation-driven modification (DDM) techniques, based on the principle of severe plastic deformation, to tailor the 80Al-5Li-5Mg-5Zn-5Cu lightweight HAA into homogeneous and refined microstructures as anode candidates for aluminum-air aqueous batteries. Magnesium (−2.4 V vs. normal hydrogen electrode (NHE)) and lithium (−3.0 V vs. NHE) elements were selected due to their higher hydrogen evolution potentials than aluminum and more positive electrode potentials than that of aluminum (−1.7 V vs. NHE) to facilitate the

* Corresponding author.
E-mail address: yxhuang@hit.edu.cn (Y. Huang).
[1] These authors contributed equally to this work.

https://doi.org/10.1016/j.scriptamat.2022.114551
1359-6462/

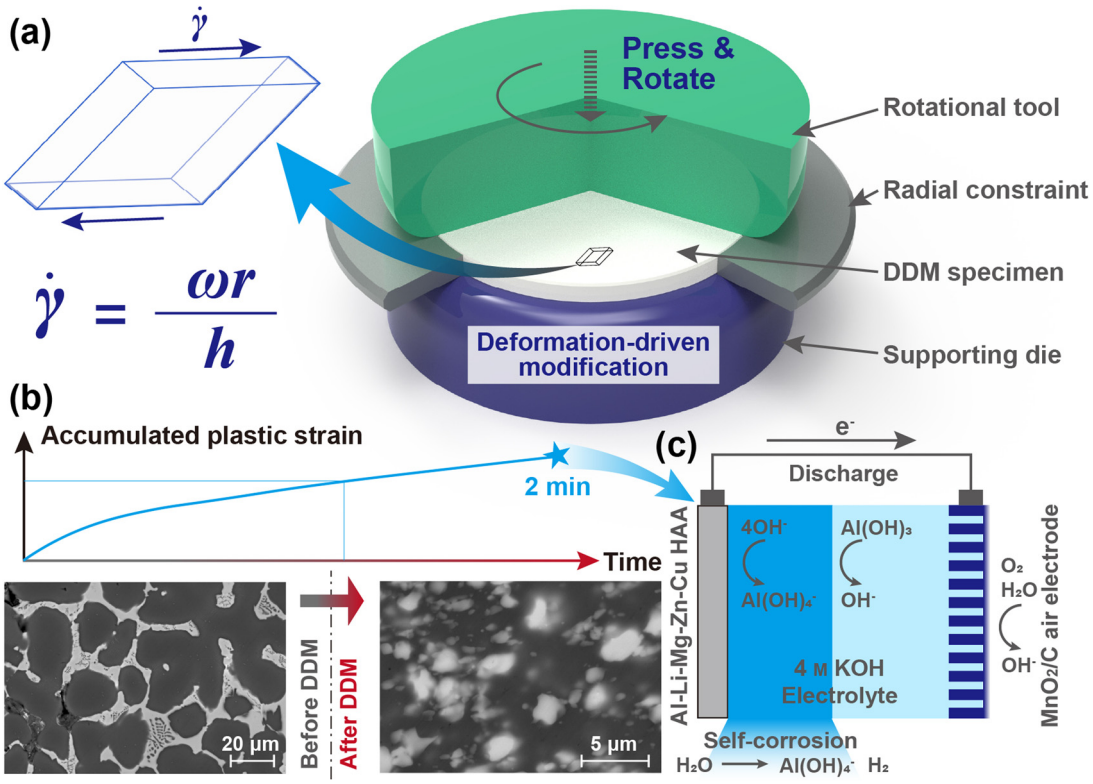

Fig. 1. Schematic illustration of preparation routes of the HAA anodes: (a) severe plastic deformation of DDM process, (b) microstructural evolution, and (c) illustration of primary aluminum-air batteries.

metal dissolution-deposition process. Zinc [25] and copper [26] elements were chosen due to their good depolarization effects. The as-cast HAA were firstly cut into discs of 16.0 mm in diameter and 2.0 mm in thickness. DDM was applied to the as-cast materials via a rotational tool with an axial pressure to compact the disc towards suppress the porosity and enhance the microstructural homogeneity, as shown in Fig. 1a. A rotational velocity of 800 rpm and a processing time of 2 min were selected. According to our previous research [27], the accumulated plastic strain applied on the modified specimens is approximately linear to the processing time. The severe plastic deformation and associated deformation/frictional heat triggered fragmentation of the precipitates [28] and dynamic recrystallization (DRX) of the grain microstructures [29]. The microstructures of HAA before/after modification are shown in Fig. 1b. Much more refined microstructures without eutectic skeletons can be seen, which avoids the severe attenuation of discharge plateau during discharging.

We explicated the discharge characteristics via a primary aluminum-air cell with the electrolyte of 4 M KOH aqueous solution without extra electrolyte additives, as shown in Fig. 1c. The air cathode was constructed by sequentially pressing the MnO_2/C catalyst layer (MnO_2:carbon black:poly tetrafluoroethylene= 1:3:1, catalyst loading 13 mg cm^{-2}), Ni-based current collector, and waterproof gas diffusion layer (mixture of Teflon and carbon-based materials). The tested anodes included as-cast and DDM HAA, and 5N pure aluminum. The discharge reactions and associated parasite reaction can be described as follows:

$$\text{Anode}: Al + 4OH^- \rightarrow Al(OH)_4^- + 3e^-;\ Al(OH)_4^- \rightarrow Al(OH)_3(s) + OH^- \quad (1)$$

$$\text{Cathode}: O_2(g) + 2H_2O + 3e^- \rightarrow 4OH^- \quad (2)$$

$$\text{Overall}: Al + 3/4O_2(g) + 3/2H_2O \rightarrow Al(OH)_3(s) \quad (3)$$

$$\text{Parasite on Anode}: Al + 3H_2O \rightarrow Al(OH)_3(s) + 3/2H_2(g) \quad (4)$$

Fig. 2a shows the discharge characteristics of these three anodes with the current density of 20, 40, 80, and 120 mA cm^{-2}. The as-cast HAA cannot even exhibit a continuous discharge plateau at the lowest discharge rate. It is attributed to the exposure of the eutectic skeletons, which cannot provide electrons to discharge. These eutectic skeletons companied by the hydroxides via anode reactions formed a dense isolation layer to prohibit continuous discharge, resulting in premature failure of discharge plateau. By contrast, the homogeneous HAA processed by DDM shows a stable discharge plateau at all current densities, confirming the fragmentation of the undesirable eutectic skeletons. The anode reaction products, hydroxides, are not absorbed by the porous framework any longer and can enter the electrolytes to prevent the formation of passivation film during discharge. The copper element distributed in homogeneously dispersed precipitates rather than in the eutectic skeletons further avoids the formation of the dense hydroxide films [30,31], contributing to a better anode-electrolyte interface for continuous discharge. Besides, with the help of magnesium and lithium elements with more positive potentials, the discharge voltage is also higher than the 5N pure aluminum. Almost no attenuation can be observed in the discharge curves of the DDM HAA specimen at 120 mAh cm^{-2}, while severe declination exists in the curves of pure aluminum, implying that the polarization effect is significantly suppressed to maintain stable discharge. The extracted power and energy densities are shown in Fig. 2b. The highest power and energy densities are obtained at the high discharge rate of 120 mAh cm^{-2}. One should note that although the copper elements in the HAA cannot offer electrons during discharge and the zinc elements have a lower theoretical energy density than the aluminum matrix [15,32], the effective energy densities of HAA are still higher than the pure aluminum. We can infer that the HER self-corrosion via parasite reaction on anodes is suppressed during discharge, which compromises the energy density loss induced by alloying elements. Hydrogen evolution mea-

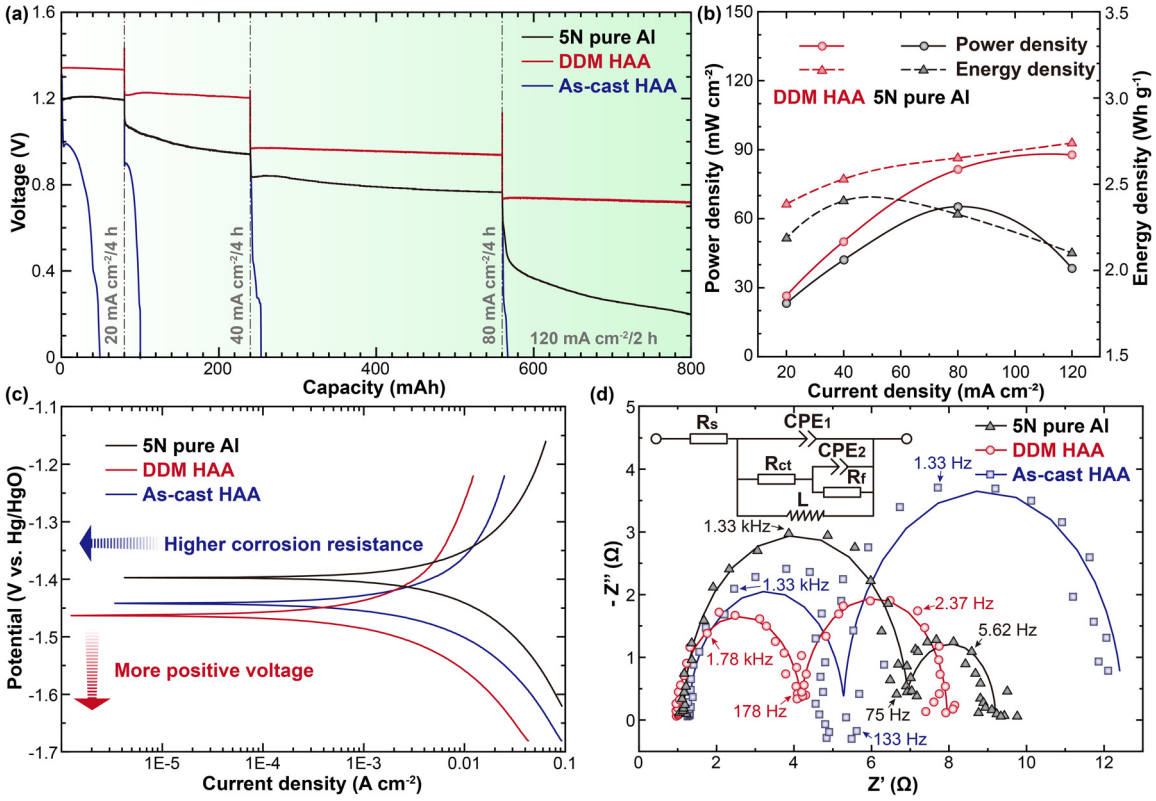

Fig. 2. Discharge characteristics and electrochemical responses: (a) discharge tests with the current densities of 20, 40, 80, and 120 mA cm^{-2}, (b) comparison of discharge performances, (c) Tafel curves, and (d) EIS responses.

Table 1
Fitted parameters of EIS results via the equivalent circuit in Fig. 2d.

		CPE_1				CPE_2		
Area	R_s (Ω cm^2)	T ($\mu\Omega^{-1}$ cm^{-2} s^n)	n	L(kH cm^{-2})	R_{ct} (Ω cm^2)	T (mΩ^{-1} cm^{-2} s^n)	n	R_f (Ω cm^2)
5N pure Al	1.2	21.8	1.00	5.4	5.8	12.1	1.00	2.3
DDM HAA	1.0	38.7	1.00	16.0	3.2	10.8	1.00	3.7
As-cast HAA	1.3	41.5	0.99	22.1	4.0	23.2	1.00	7.2

surement of these three anodes in 4 m KOH aqueous solution was conducted via Archimedes drainage method. The obtained hydrogen evolution rates of as-cast HAA, DDM HAA, and 5N pure aluminum are 9.86 ± 0.61, 0.57 ± 0.23, and 3.72 ± 0.25 mL cm^{-2} h^{-1}, respectively. The porosity existing in the as-cast microstructures enlarge the exposure area to the alkaline solution, resulting in a drastic HER process. After DDM, the corrosion rate is significantly suppressed to mitigate the undesirable parasite reaction rate, only about one-seventh of pure aluminum. As such, these elements can effectively increase the discharge voltage, alleviate polarization, and avoid the formation of the passivation film.

The electrochemical responses, including potentiodynamic polarization (PDP) and electrochemical impedance (EIS) tests were conducted via CHI 760E and PARSTAT 4000A electrochemical workstations. Fig. 2c shows the Tafel curves of three kinds of anodes with a scanning rate of 1 mV s^{-1}. The existence of positive elements results in a more negative corrosion potential vs. Hg/HgO reference electrode (more positive voltage) than the pure aluminum. However, due to the anodic protection effect of active elements of magnesium, the self-corrosion rate is suppressed, resulting in higher corrosion resistance than pure aluminum. The EIS results and the associated equivalent circuit is shown in Fig. 2d. Table 1 shows the fitted electronic component parameters. The DDM HAA has the lowest charge transfer resistance R_{ct} value (3.2 Ω cm^2) among the three kinds of anodes, indicating the strongest characteristics as electron donors. The activation of the DDM HAA anode by the high alloying and severe plastic deformation process contributes to the high discharge voltage. The film resistance of this anode is also higher since the corresponding R_f value is a bit higher than that of pure aluminum, which is responsible for the overall good corrosion resistance (low HER rate). In addition, since the n values of all Q_2 are 1.00, these Q_2 can be regarded as the ideal capacitance element. One can see that the T value of Q_2 of as-cast HAA is much higher than that of the severe plastic deformation-modified specimens, proving that the eutectic skeleton-induced dense passivation film is avoided by the homogenized microstructures.

To further illustrate the effect of severe plastic deformation on the discharge characteristics, we conducted electron backscattered diffraction (EBSD) observation via a HITACHI SU5000 scanning electron microscope (SEM) equipped with an Oxford Instrument C-Nano EBSD detector, as shown in Fig. 3. The as-cast HAA exhibits a typical dendrite structure with eutectic skeletons distributed intergranularly in the inversed pole figures (IPF). After the modification via severe plastic deformation, the grain morphologies show an equiaxed structure with an average grain diameter of 3.37 ± 2.27 μm. The high plastic strain introduced by the DDM process increases the local geometrical necessary dislocation den-

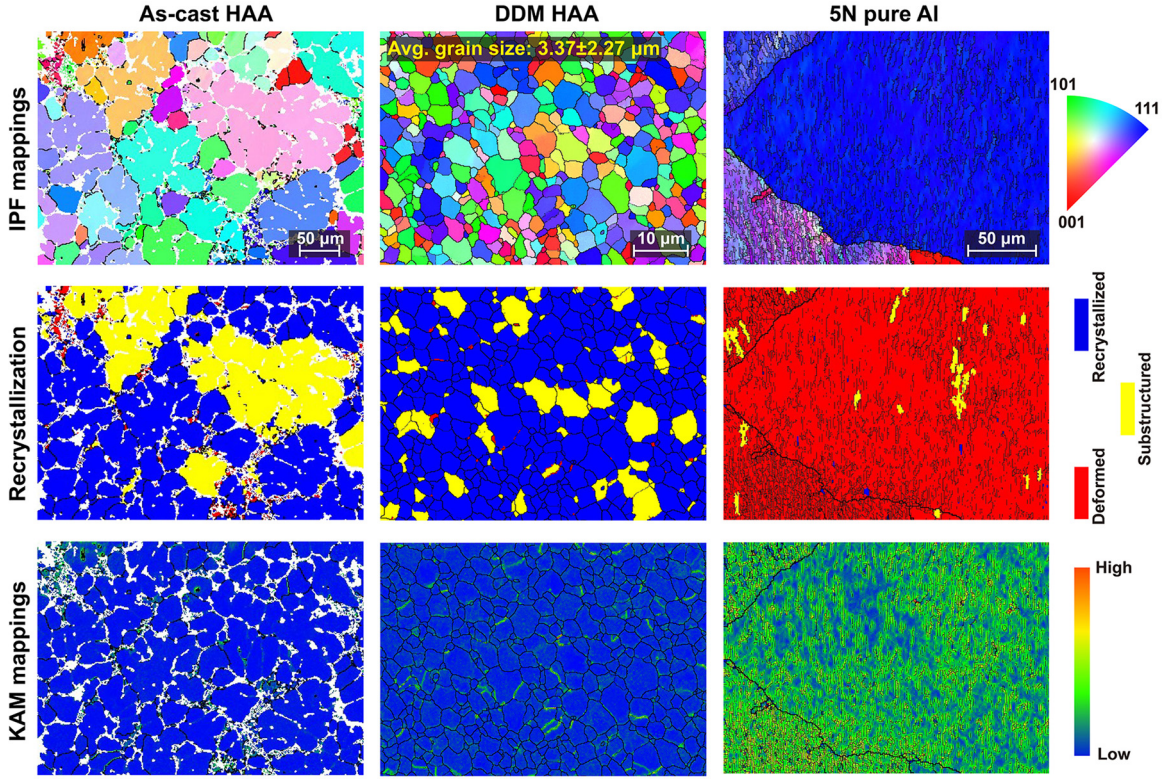

Fig. 3. Grain morphologies of three kinds of anodes via EBSD techniques.

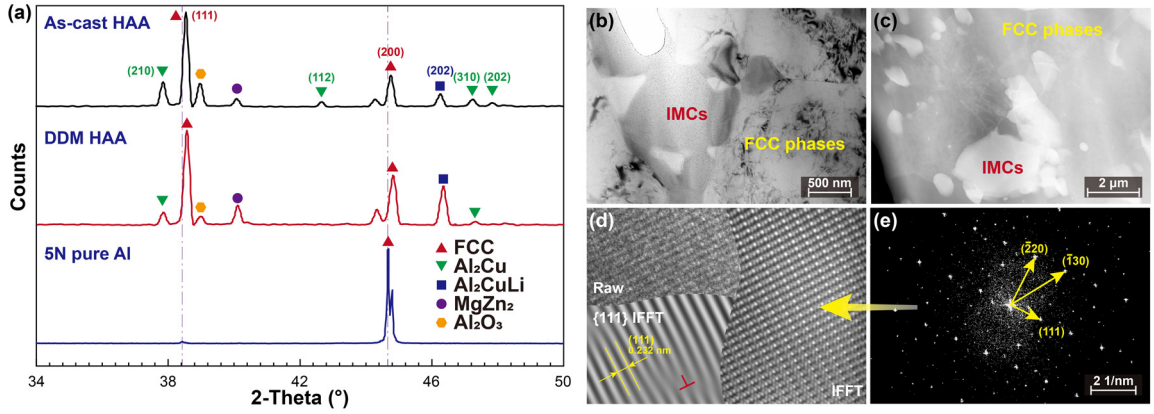

Fig. 4. Microstructural factors of three kinds of anodes via EBSD techniques: (a) XRD results, and (b) bright-field image, (c) dark-field image, (d) high-resolution image with inversed fast Fourier transform, and (e) SAED results via TEM observation.

sities. These unevenly distributed strain hardening within the HAA brings about the localization of material flow, leading to the dislocation pile-up gradually forming a series of dislocation walls. The further accumulation of plastic strain causes the angle between two adjacent grains to increase and triggers the formation of sub-grain boundaries. These sub-grain boundaries and substructures continue to grow with the help of continuous plastic deformation input to finally form the equiaxed grain structures. Due to the sufficient heat input, the residual geometrical necessary dislocation densities are not obvious, as seen in the kernel average misorientation (KAM) mappings. This phenomenon weakens the lattice distortion of the modified HAA to avoid the local corrosion promotion activity [33]. The obtained ultrafine-grained microstructures further inhibit the heterogeneity to ensure the continuous discharge and low HER rate. By contrast, the 5N pure aluminum depicts a coarse grain structure with high geometrical necessary dislocation densities induced by the cold rolling process. The excessive defect energies bring about a higher self-corrosion rate, which decreases the durability of the pure aluminum in primary aluminum-air batteries.

X-ray diffraction (XRD, PANalytical X'PERT) and transmission electron microscopy (TEM, Thermo Scientific Talos, working voltage 200 kV) were applied to the anodes to show the phase evolution during the DDM process. The peak associated with Al_2O_3 gradually decreases, which indicates that the undesired oxide film in the as-cast materials is broken (Fig. 4a). The ratio of the $T_1(Al_2CuLi)$ phase increases while the ratio of θ (Al_2Cu) decreases. This implies that partial θ phases react with the lithium-rich phases to form the T_1 phase during severe plastic deformation [34]. The T_1 phase containing lithium elements is more anodic than the θ phase [35], which may help the stable discharge. The TEM images (Fig. 4b) also confirm the homogeneity of the microstructure. No connective pre-

cipitate skeletons can be found, which suppresses the formation of undesirable passivation films. As such, the stable discharge plateau with high voltage was obtained in the DDM HAA with homogeneous microstructures.

In conclusion, we demonstrated that the deformation-driven modified Al-Li-Mg-Zn-Cu high-alloy aluminum exhibited a more stable discharge plateau and higher voltage than pure aluminum in primary aluminum-air batteries. Homogeneous microstructures induced by the fragmentation of second phases and dynamic recrystallization suppressed the formation of the hydroxides-eutectic skeletons to isolate anodes from alkaline electrolytes. The addition of copper elements further avoided the formation of the dense hydroxide films, which realized the continuous discharge. Magnesium, zinc, and lithium elements contributed to the inhibition of hydrogen evolution self-corrosion, the mitigation of polarization, and the enhancement of the discharge voltage. No attenuation was observed in the discharge curves of severe plastic deformation-modified high-alloy aluminum anodes at 120 mAh cm^{-2}. The self-corrosion rate was only one-seventh of the 5N pure aluminum. The power and energy densities reached 88.3 mW cm^{-2} and 2.73 Wh g^{-1}, respectively, which is obviously better than those of pure aluminum. This strategy is significant for designing high-performance aluminum anodes for high-power-density applications.

Data availability

The data that support the findings of this study are available from the corresponding author upon reasonable request.

Declaration of Competing Interest

The authors declare that they have no known competing financial interests or personal relationships that could have appeared to influence the work reported in this paper.

Acknowledgement

This work was jointly supported by the Heilongjiang Postdoctoral Foundation (No. LBH-Z20055), and the National Natural Science Foundation of China (No. 52175301).

References

[1] S. Mallapaty, Nature 586 (2020) 482–483.
[2] M. Li, J. Lu, Z. Chen, K. Amine, Adv. Mater. 30 (2018) 1800561.
[3] D.P. Finegan, J. Zhu, X. Feng, M. Keyser, M. Ulmefors, W. Li, M.Z. Bazant, S.J. Cooper, Joule 5 (2021) 316–329.
[4] J. Yu, B.Q. Li, C.X. Zhao, Q. Zhang, Energy Environ. Sci. 13 (2020) 3253–3268.
[5] W. Ling, H. Wang, Z. Chen, Z. Ji, J. Wang, J. Wei, Y. Huang, Adv. Funct. Mater. 31 (2021) 2006855.
[6] X. Liu, P. Zhang, J. Xue, C. Zhu, X. Li, Z. Wang, Chem. Eng. J. 417 (2021) 128006.
[7] B.J. Hopkins, Y. Shao-Horn, D.P. Hart, Science 362 (2018) 658–661.
[8] S. Choi, H.W. Do, D. Jin, S. Kim, J. Lee, A. Soon, J. Moon, W. Shim, Adv. Funct. Mater. 31 (2021) 2101720.
[9] C. Zhang, Z. Cai, R. Wang, P. Yu, H. Liu, Z. Wang, J. Electrochem. Soc. 168 (2021) 030519.
[10] J. Ren, C. Fu, Q. Dong, M. Jiang, A. Dong, G. Zhu, J. Zhang, B. Sun, ACS Sustain. Chem. Eng. 9 (2021) 2300–2308.
[11] L. Fan, H. Lu, J. Leng, Z. Sun, J. Electrochem. Soc. 162 (2015) A2623–A2627.
[12] R. Buckingham, T. Asset, P. Atanassov, J. Power Sour. 498 (2021) 229762.
[13] J. Ryu, M. Park, J. Cho, Adv. Mater. 31 (2019) 1804784.
[14] N. Dong, H. Luo, Y. Xia, H. Guo, R. Fu, Z. Liu, Chem. Commun. 55 (2019) 2352–2355.
[15] M. Deng, L. Wang, B. Vaghefinazari, W. Xu, C. Feiler, S.V. Lamaka, D. Höche, M.L. Zheludkevich, D. Snihirova, Energy Storage Mater. 43 (2021) 238–247.
[16] I.J. Park, S.R. Choi, J.G. Kim, J. Power Sour. 357 (2017) 47–55.
[17] Z. Sun, H. Lu, J. Electrochem. Soc. 162 (2015) A1617–A1623.
[18] Z. Wu, H. Zhang, S. Tang, J. Zou, D. Yang, Y. Wang, K. Qin, C. Ban, J. Cui, H. Nagaumi, Electrochim. Acta 370 (2021) 137833.
[19] X. Lan, H. Wang, Z. Sun, X. Jiang, J. Alloys Compd. 805 (2019) 942–946.
[20] M. Jiang, C. Fu, P. Meng, J. Ren, J. Wang, J. Bu, A. Dong, J. Zhang, W. Xiao, B. Sun, Adv. Mater. 34 (2021) 2102026.
[21] T. Wang, J.E. Atehortua, M. Song, M. Reza-E-Rabby, B.S. Taysom, J. Silverstein, T. Roosendaal, D. Herling, S. Whalen, Mater. Des. 213 (2022) 110374.
[22] T. Wang, B. Gwalani, J. Silverstein, J. Darsell, S. Jana, T. Roosendaal, A. Ortiz, W. Daye, T. Pelletiers, S. Whalen, Materials 13 (2020) 5333 Basel.
[23] M. Paidar, D. Bokov, S. Mehrez, O.O. Ojo, V.V. Ramalingam, S. Memon, Surf. Coat. Technol. 426 (2021) 127797.
[24] Y. Xie, X. Meng, Y. Chang, D. Mao, Y. Yang, Y. Xu, L. Wan, Y. Huang, Compos. Sci. Technol. 219 (2022) 109225.
[25] C. Yan, C. Lv, L. Wang, W. Cui, L. Zhang, K.N. Dinh, H. Tan, C. Wu, T. Wu, Y. Ren, J. Chen, Z. Liu, M. Srinivasan, X. Rui, Q. Yan, G. Yu, J. Am. Chem. Soc. 142 (2020) 15295–15304.
[26] Y. Liu, M.A. Arenas, S.J. Garcia-Vergara, T. Hashimoto, P. Skeldon, G.E. Thompson, H. Habazaki, P. Bailey, T.C.Q. Noakes, Corros. Sci. 50 (2008) 1475–1480.
[27] Y. Xie, X. Meng, Y. Li, D. Mao, L. Wan, Y. Huang, Compos. Commun. 26 (2021) 100776.
[28] Y. Xie, X. Meng, D. Mao, Z. Qin, L. Wan, Y. Huang, ACS Appl. Mater. Interfaces 13 (2021) 32161–32174 acsami.1c07148.
[29] T. Sakai, A. Belyakov, R. Kaibyshev, H. Miura, J.J. Jonas, Prog. Mater. Sci. 60 (2014) 130–207.
[30] L. Mei, X.P. Chen, C. Wang, J. Xie, Q. Liu, Mater. Charact. 181 (2021) 111469.
[31] Y. Xie, X. Meng, F. Wang, Y. Jiang, X. Ma, L. Wan, Y. Huang, Corros. Sci. 192 (2021) 109800.
[32] C. Li, Y. Sun, F. Gebert, S. Chou, Adv. Energy Mater. 7 (2017) 1700869.
[33] W. Sun, Y. Yang, Z. Yang, L. Wang, J. Wang, D. Xu, G. Liu, J. Mater. Sci. Technol. 91 (2021) 278–306.
[34] Y. Xie, X. Meng, R. Zang, Y. Chang, L. Wan, Y. Huang, Mater. Sci. Eng. A 830 (2022) 142332.
[35] R.G. Buchheit, J. Electrochem. Soc. 142 (1995) 3994–3996.